

1 **LES Modeling of Tsunami-like Solitary Wave Processes**
2 **over Fringing Reefs**

3

4 Yu Yao^{1,4}, Tiancheng He¹, Zhengzhi Deng^{2*}, Long Chen^{1,3}, Huiqun Guo¹

5

6 ¹ School of Hydraulic Engineering, Changsha University of Science and Technology,
7 Changsha, Hunan 410114, China.

8 ² Ocean College, Zhejiang University, Zhoushan, Zhejiang 316021, China.

9 ³ Key Laboratory of Water-Sediment Sciences and Water Disaster Prevention of
10 Hunan Province, Changsha 410114, China.

11 ⁴Key Laboratory of Coastal Disasters and Defence of Ministry of Education,
12 Nanjing, Jiangsu 210098, China

13

14

15

16 * Corresponding author: Zhengzhi Deng

17 E-mail: zzdeng@zju.edu.cn

18 Tel: +86 15068188376

19

20 **ABSTRACT**

21 Many low-lying tropical and sub-tropical reef-fringed coasts are vulnerable to
22 inundation during tsunami events. Hence accurate prediction of tsunami wave
23 transformation and runup over such reefs is a primary concern in the coastal management
24 of hazard mitigation. To overcome the deficiencies of using depth-integrated models in
25 modeling tsunami-like solitary waves interacting with fringing reefs, a three-dimensional
26 (3D) numerical wave tank based on the Computational Fluid Dynamics (CFD) tool
27 OpenFOAM® is developed in this study. The Navier-Stokes equations for two-phase
28 incompressible flow are solved, using the Large Eddy Simulation (LES) method for
29 turbulence closure and the Volume of Fluid (VOF) method for tracking the free surface.
30 The adopted model is firstly validated by two existing laboratory experiments with
31 various wave conditions and reef configurations. The model is then applied to examine
32 the impacts of varying reef morphologies (fore-reef slope, back-reef slope, lagoon width,
33 reef-crest width) on the solitary wave runup. The current and vortex evolutions associated
34 with the breaking solitary wave around both the reef crest and the lagoon are also
35 addressed via the numerical simulations.

36

37 **Keywords:** Solitary wave; wave transformation, wave runup; fringing reef; LES.

38

39 **1 Introduction**

40 Tsunami is an extremely destructive natural disaster, which can be generated by
41 earthquakes, landslides, volcanic eruptions, and meteorite impacts. Tsunami damage
42 occurs mostly in the coastal areas where tsunami waves runup or rundown the beach,
43 overtop or ruin the coastal structures, and inundate the coastal towns and villages (Yao et
44 al., 2015). Some tropic and sub-tropic coastal areas vulnerable to tsunami hazards are
45 surrounded by coral reefs, especially those in the Pacific and Indian Oceans. Among
46 various coral reefs, fringing reefs are the most common type. A typical cross-shore
47 fringing reef profile can be characterized by a steep offshore fore-reef slope and an
48 inshore shallow reef flat (Gourlay, 1996). There is also possibly a reef crest lying at the
49 reef edge (e.g., Hench et al., 2008) and/or a narrow shallow lagoon existing behind the
50 reef flat (e.g., Lowe et al., 2009a). Over decades, fringing reefs have been well
51 recognized to be able to shelter low-lying coastal areas from flood hazards associated
52 with storms and high surf events (e.g. Cheriton et al. 2016; Lowe et al., 2005; Lugo-
53 Fernandez et al., 1998; Péquignet et al., 2011; Young, 1989). However, until after the
54 2004 Indian Ocean Tsunami, the positive role of coral reefs in mitigating the tsunami
55 waves has begun to arise the attentions of the scholars who conducted the post-disaster
56 surveys (e.g., Chatenoux and Peduzzi, 2007; Ford et al., 2014; Mcadoo et al., 2011).
57 There is consensus among the **researchers** that in addition to establish the global tsunami
58 warning system, the cultivation of coastal vegetation (mangrove forest, coral reef, etc.) is
59 also one of the coastal defensive measures against the tsunami waves (e.g., Dahdouh-
60 Guebas et al., 2006; Danielsen et al., 2005; Mcadoo et al., 2011). Numerical models have
61 been proven to be powerful tools to investigate tsunami wave interaction with the
62 mangrove forests (e.g., Huang et al., 2011; Maza et al., 2015; Tang et al., 2013 and many
63 others). Comparatively speaking, their applications in modeling coral reefs subjected to
64 tsunami waves are still very few.

65 Over decades, modeling wave processes over reef profiles faces several challenges
66 such as steep fore-reef slope, complex reef morphology as well as spatially-varied surface
67 roughness. Local but strong turbulence due to wave breaking in the vicinity of reef edge
68 needs to be resolved. Among various approaches for modelling wave dynamics over reefs,
69 two groups of models are the most pervasive. The first group focuses on using the phase-

70 averaged wave models and the nonlinear shallow water equations to model the waves and
71 the flows, respectively, in field reef environments, and typically the concept of radiation
72 stress (Longuet-Higgins and Stewart, 1964) or vortex-force (Craig and Leibovich, 1976)
73 is used to couple the waves and the flows (e.g., Douillet et al., 2001; Kraines et al., 1998;
74 Lowe et al., 2009b, 2010; Van Dongeren et al., 2013; Quataert et al., 2015). As for
75 modeling tsunami waves at a field scale, we are only aware of in the literature that
76 Kunkel et al. (2006) implemented a nonlinear shallow water model to study the effects of
77 wave forcing and reef morphology variations on the wave runup. However, their
78 numerical model was not verified by any field observations. The second group aims at
79 using the computationally efficient and phased-resolving model based on the Boussinesq
80 equations. This depth-integrated modeling approach employs a polynomial
81 approximation to the vertical profile of velocity field, thereby reducing the dimensions of
82 a three-dimensional problem by one. It is able to account for both nonlinear and
83 dispersive effects at intermediate water level. At a laboratory scale, Boussinesq models
84 combined with some semi-empirical breaking-wave and bottom friction models have
85 been proven to be able to simulate the motions of regular waves (Skotner and Apelt, 1999;
86 Yao et al., 2012), irregular waves (Nwogu and Demirbilek, 2010; Yao et al., 2016, 2019)
87 and infragravity waves (Su et al., 2015; Su and Ma, 2018) over fringing reef profiles.

88 The solitary wave has been employed in many laboratory/numerical studies to model
89 the leading wave of a tsunami. Compared to the aforementioned regular/irregular waves,
90 the numerical investigations of solitary wave interaction with the laboratory reef profile
91 are much fewer. Roeber and Cheung (2012) was the pioneer study to simulate the solitary
92 wave transformation over a fringing reef using a Boussinesq model. Laboratory
93 measurements of the cross-shore wave height and current across the reef as conducted by
94 Roeber (2010) were reproduced by their model. More recently, Yao et al. (2018) also
95 validated a Boussinesq model based on their laboratory experiments to assess the impacts
96 of reef morphologic variations (fore-reef slope, back-reef slope, reef-flat width, reef-crest
97 width) on the solitary wave runup over the back-reef beach. Despite of above applications,
98 several disadvantages still exist in using the Boussinesq-typed models: (1) Boussinesq
99 equations are subjected to the mild-slope assumption, thus it is questionable when using
100 for reefs with steep fore-reef slope, particularly when there is a sharp reef crest locating at

101 the reef edge; (2) wave breaking could not be inherently captured by Boussinesq-type
102 models thus empirical breaking model or special numerical treatment is usually needed;
103 (3) Boussinesq models could not resolve the vertical flow structure associated with the
104 breaking waves due to the polynomial approximation to the vertical velocity profile.

105 To remedy the above deficiencies of using Boussinesq-typed models to simulate the
106 solitary processes (wave breaking, bore propagation, and runup) over the fringing reefs,
107 we develop a 3D numerical wave tank based on the CFD tool OpenFOAM® (Open Field
108 Operation and Manipulation) in this study. OpenFOAM® is a widely used open-source
109 CFD code in the modern industry supporting two-phase incompressible flow (via its
110 solver interFoam). With appropriate treatment of wave generation and absorption, it has
111 been proved to be a powerful and efficient tool for exploring complicated nearshore wave
112 dynamics (e.g., Higuera et al., 2013b). In this study, the Navier–Stokes equations for an
113 incompressible fluid are solved. For the turbulence closure model, although LES
114 demands more computational resources than RANS, it computes the large-scale unsteady
115 motions explicitly. Importantly, it could provide more statistical information for the
116 turbulence flows in which large-scale unsteadiness is significant (Pope, 2000). Thus the
117 LES model is adopted by considering that the breaking-wave driven flow around the reef
118 edge/crest is fast and highly unsteady. The free surface motions are tracked by the widely
119 used VOF method.

120 In this study, we first validate the adopted model by the laboratory experiments of
121 Roeber (2010) as well as our previous experiments (Yao et al., 2018). The robustness of
122 the present model in reproducing such solitary wave processes as wave breaking near the
123 reef edge/crest, turbulence bore propagating on the reef flat and wave runup on the back-
124 reef beach, is demonstrated. The model is then applied to investigate the impacts of
125 varying reef morphologies (fore-reef slope, back-reef slope, lagoon width, reef crest
126 width) on the solitary wave runup. The flow and vorticity fields associated with the
127 breaking solitary wave around the reef crest and the lagoon are also analyzed by the
128 model results. The rest of this paper is organized as follows. The numerical model is
129 firstly described in Section 2. It is then validated by the laboratory data from the literature
130 as well as our data in Section 3. What follows in Section 4 are the model applications for

131 which laboratory data are unavailable. The main conclusions drawn from this study are
 132 given in Section 5.

133 **2 Numerical Methods**

134 **2.1 Governing equations**

135 To simulate breaking-wave processes across the reef, the LES approach is employed
 136 to balance the need of resolving a large portion of the turbulent flow energy in the
 137 domain while parameterizing the unresolved field with a subgrid closure in order to
 138 maintain a reasonable computational cost. The filtered Navier-Stokes equations is
 139 essential to separate the velocity field that contains the large-scale components, which is
 140 performed by filtering the velocity field (Leonard, 1975). The filtered velocity **in the i-th**
 141 **spatial coordinate** is defined as

$$142 \quad \bar{u}_i(x) = \int G(x, x') u_i(x') dx' \quad (1)$$

143 where $G(x, x')$ is the filter kernel, which is a localized function. The eddy sizes are
 144 identified using a characteristic length scale, Δ , which is defined as

$$145 \quad \Delta = (\Delta x \cdot \Delta y \cdot \Delta z)^{1/3} \quad (2)$$

146 where Δx , Δy , Δz are the grid size in streamlines, spanwise and vertical directions,
 147 respectively. Eddies that are larger than Δ are roughly considered as large eddies, and
 148 they are directly solved. Those who are smaller than Δ are small eddies.

149 **For incompressible flow, the** filtered continuity and momentum equations are as
 150 follows

$$151 \quad \frac{\partial \bar{u}_i}{\partial x_i} = 0 \quad (3)$$

$$152 \quad \frac{\partial \rho \bar{u}_i}{\partial t} + \frac{\partial (\rho \bar{u}_i \bar{u}_j)}{\partial x_j} = -\frac{\partial \bar{p}}{\partial x_i} + \rho g_i + 2\mu \frac{\partial \bar{S}_{ij}}{\partial x_j} - \frac{\partial \tau_{ij}^r}{\partial x_j} \quad (4)$$

153 where ρ **is the water density**, μ **is the dynamic viscosity**, \bar{p} is the filtered pressure, \bar{S}_{ij}
 154 is the strain rate of the large scales defined as

$$155 \quad \bar{S}_{ij} = \frac{1}{2} \left(\frac{\partial \bar{u}_i}{\partial x_j} + \frac{\partial \bar{u}_j}{\partial x_i} \right) \quad (5)$$

156 and τ_{ij}^r is the residual stress approximated by using sub-grid scale (SGS) models to get a
 157 full solution for the Navier-Stokes equations.

158 The **residual** stress is usually calculated by a linear relationship with the rate of
 159 strain tensor based on the Boussinesq hypothesis. The one-equation eddy viscosity mode,
 160 which is supposed to be better than the well-known Smagorinsky model for solving the
 161 highly complex flow and shear flow (Menon et al., 1996), is employed in the present
 162 study. Based on the one-equation model (Yoshizawa and Horiuti, 1985), the sub-grid
 163 stresses are defined as

$$164 \quad \tau_{ij}^r = \frac{2}{3} k_s \delta_{ij} - 2\nu_t (\bar{S}_{ij} - \frac{1}{3} \bar{S}_{kk} \delta_{ij}) \quad (6)$$

165 where δ_{ij} is the Kronecker-delta, and ν_t is the SGS eddy viscosity, which is given by
 166

$$\nu_t = C_k \Delta \sqrt{k_s} \quad (7)$$

167 and the SGS kinetic energy k_s needs to be solved by

$$168 \quad \frac{\partial k_s}{\partial t} + \bar{u}_i \frac{\partial k_s}{\partial x_i} = \frac{\partial}{\partial x_i} \left(\frac{\mu}{P_r} \frac{\partial k_s}{\partial x_i} \right) - \frac{\tau_{ij}^r}{\rho} \frac{\partial \bar{u}_j}{\partial x_i} - \frac{C_\varepsilon k_s^{3/2}}{\Delta} \quad (8)$$

169 where $C_k = 0.094$, $C_\varepsilon = 0.916$ and $P_r = 0.9$ as suggested by the OpenFOAM® User
 170 Guide (2013).

171 The **presence of the free-surface interface between the air and water is treated**
 172 **through the commonly used VOF method (Hirt and Nichols, 1981), which introduces a**
 173 **volume fraction and solves an additional modeled transport equation for this quantity.**
 174 The general representation of fluid density ρ is written as

$$175 \quad \rho = \alpha \rho_1 + (1 - \alpha) \rho_2 \quad (9)$$

176 where $\rho_1 = 1000 \text{ kg} / \text{m}^3$ is the density of water, $\rho_2 = 1 \text{ kg} / \text{m}^3$ is the density of air, α is
 177 the volume fraction of water contained in a grid cell. The distribution of α is modeled by
 178 **the** advection equation

$$179 \quad \frac{\partial \alpha}{\partial t} + \nabla \cdot (\alpha \bar{u}_i) + \nabla \cdot [\alpha (1 - \alpha) u_i'] = 0 \quad (10)$$

180 The last term on the left side is an artificial compression term, avoiding the excessive
 181 numerical diffusion and the interface smearing, the new introduced u_i^r is a velocity field
 182 suitable to compress the interface.

183 In the present solver interFoam, the algorithm PIMPLE, which is a mixture of the
 184 PISO (Pressure Implicit with Splitting of Operators) and SIMPLE (Semi-Implicit Method
 185 for Pressure-Linked Equations) algorithms, is employed to solve the coupling of velocity
 186 and pressure fields. The MULES (multi-dimensional universal limiter for explicit
 187 solution) method is used to maintain boundedness of the volume fraction independent of
 188 the underlying numerical scheme, mesh structure, *etc.* Euler scheme is utilized for the
 189 time derivatives, Gauss linear scheme is used for gradient term, and Gauss linear
 190 corrected scheme is selected for the Laplacian term. Detailed implementation can be
 191 founded in the OpenFOAM® User Guide (2013).

192 **2.2 Wave generation and absorption**

193 Wave generation and absorption are essentials for a numerical wave tank, but they
 194 are not included in the official version of OpenFOAM®. Therefore, supplementary
 195 modules were developed by the other users, e.g., waves2Foam (Jacobsen et al., 2012) and
 196 IH-FOAM (Higuera et al., 2013a). In this study, the IH-FOAM is selected in that it
 197 employs an active wave absorbing boundary and does not require an additional relaxation
 198 zone as used by waves2Foam. Meanwhile, it supports many wave theories including the
 199 solitary wave theory. The free surface and velocity for a solitary wave generation in IH-
 200 FOAM are (Lee et al., 1982)

$$201 \quad \eta = H \operatorname{sech}^2 \left(\sqrt{\frac{3H}{4h^3}} X \right) \quad (11)$$

$$202 \quad \frac{u}{\sqrt{gh}} = \frac{\eta}{h} \left[1 - \frac{1}{4} \frac{\eta}{h} + \frac{h}{3\eta} \left(1 - \frac{3}{2} \frac{z^2}{h^2} \right) \frac{d^2\eta}{dX^2} \right] \quad (12)$$

$$203 \quad \frac{w}{\sqrt{gh}} = \frac{-z}{h} \left[\left(1 - \frac{1}{2} \frac{\eta}{h} \right) \frac{d\eta}{dX} + \frac{1}{3} h^2 \left(1 - \frac{1}{2} \frac{z^2}{h^2} \right) \frac{d^3\eta}{dX^3} \right] \quad (13)$$

204 where η is the free surface elevation, H is the wave height, h is the water depth,
205 $X = x - ct$, $c = \sqrt{g(h+H)}$ is the wave celerity, u and w are the velocities in the
206 streamwise and vertical directions, respectively.

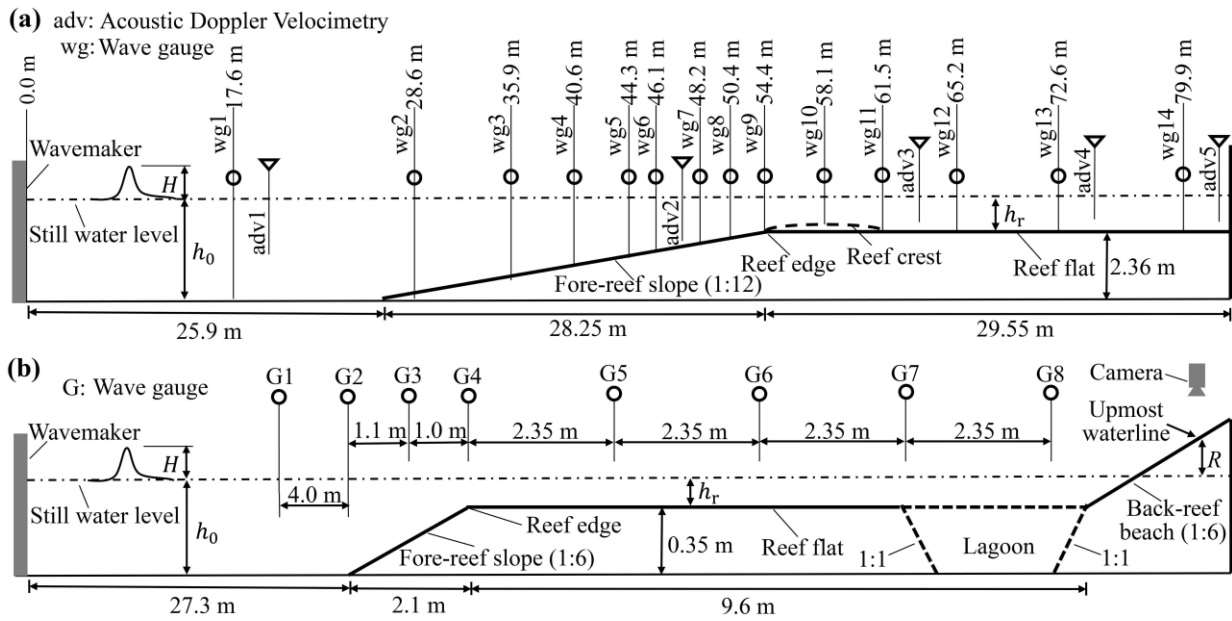
207 **3 Model validation**

208 **3.1 Experimental settings**

209 The first set of laboratory experiments serving as validation purpose is Roeber (2010),
210 who reported two series of experiments conducted at Oregon State University, U.S.A. in
211 separate wave flumes. In this study, we only reproduce their experiments in the large
212 wave flume, which is 104 m long, 3.66 wide and 4.57 m high. As illustrated in Fig. 1a,
213 the two-dimensional (2D) reef model, starting at 25.9 m from the wavemaker, was built
214 by a plane fore-reef slope attached to a horizontal reef flat of 2.36 m high followed by a
215 back-reef vertical wall. Both the waves and flows across the reef profile were measured
216 by 14 wave gauges (wg1-wg14) and 5 ADVs (Acoustic Doppler velocimeters),
217 respectively. Only two scenarios for the reef with and without a trapezoidal reef crest
218 subjected to two incident waves are reported in this study (see also Table 1). The large
219 wave flume experiments facilitate us to test our model's ability to handle relatively large-
220 scale nonlinear dispersive waves together with wave breaking, bore propagation and
221 associated wave-driven flows. For more detailed experimental setup, see Roeber (2010).

222 The second set of 2D reef experiments for model validation comes from our
223 previous work (Yao et al., 2018). These experiments were conducted in a small wave
224 flume 40 m long, 0.5 m wide and 0.8 m high at Changsha University of Science and
225 Technology, P. R. China. As shown in Fig. 1b, a plane slope was built at 27.3 m from the
226 wavemaker and it was truncated by a horizontal reef flat of 0.35 m high. A back-reef
227 beach of 1:6 was attached to the end of the reef flat. The surface elevations were
228 measured at 8 cross-shore locations (G1-G8) and no flow measurement was performed.
229 However, A CCD camera was installed to record the process of water uprush on the
230 back-reef slope. Thus the model's robustness to capture the whole process of solitary

231 wave transformation over the reef flat and runup on the back-reef beach can be evaluated.
 232 In this study, we only simulate the tested idealized reef profile with and without a lagoon
 233 at the rear of reef flat subjected to the same wave condition (see also Table 1). The
 234 lagoon was formed by two 1:1 slope connecting the reef flat and the toe of the back-reef
 235 beach to the flume bottom, respectively. **The dimensions of the fore-reef slope and the**
 236 **reef flat, the water depths over the reef flat, and the incoming wave heights were designed**
 237 **according to the Froude similarity with a target geometric scale factor of 1:20.** See Yao et
 238 al. (2018) for the detailed laboratory settings.



239 Fig. 1 Experiment settings for: (a) Roeber (2010) and (b) Yao et al. (2018).

240 Table 1 Reef configuration and wave condition for the tested scenarios

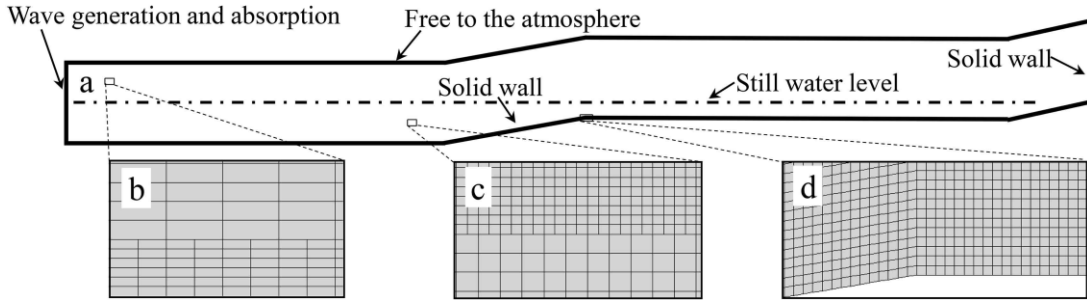
Scenario I.D.	Offshore wave height H_0 (m)	Offshore water depth h_0 (m)	Reef-flat water depth h_r (m)	Fore-reef slope s	Reef-flat length L_r (m)	Reynolds number Re at the breaking point	Remarks	Source
1	1.23	2.46	0.1	1:12	29.5	5.9×10^7	–	Roeber (2010)
2	0.75	2.5	0.14	1:12	22.8	1.4×10^7	With reef crest	Roeber (2010)
3	0.08	0.40	0.05	1:6	9.6	2.4×10^5	–	Yao et al. (2018)
4	0.08	0.40	0.05	1:6	8.0	2.4×10^5	With lagoon	Yao et al. (2018)

241 3.2 Numerical settings

242 By considering a balance between the computational accuracy and efficiency, the
243 computational domain (Fig. 2a) is designed to reproduce the main aspects of the
244 laboratory settings. We calibrate the model in the principle that the computed leading
245 solitary wave height at the most offshore gauge should exactly reproduce its
246 measurement. For a solitary wave, wave length (L) can be estimated as a distance
247 containing 95% of the total mass of the solitary wave, which yields $L = 2.12h / \sqrt{H_i / h}$.
248 The largest offshore wave length according to the wave conditions in Table 1 is $L = 8.44$
249 m/1.52 m for the scenario of Roeber (2010)/Yao et al. (2018). Thus, we reasonably put
250 the numerical wave generation and absorption at a location 15 m/6 m from the toe of
251 fore-reef slope, which is also the location of left boundary. Behind the reef flat,
252 transmitted waves are allowed to runup on the back-reef beach, but they cannot overtop
253 out of the computational domain due to a solid wall condition at the right boundary. In
254 addition, we set the “free to the atmosphere” for the top boundary. For the two side faces,
255 we employed the “empty” boundary in OpenFOAM to simulate the 2D reef
256 configurations. **When solitary waves interact with the investigated laboratory reefs,**
257 **strong turbulence is expected to be generated inside the domain where wave breaks near**
258 **the reef crest and propagates on the reef flat as a moving bore, thus we do not set the**
259 **inflow boundary condition with desired turbulence characteristics for the LES at the wave**
260 **generation boundary. Meanwhile, since both the laboratory reef surfaces are very smooth,**
261 **the flow structure near the bottom is not resolved in our simulations, and we only impose**
262 **a no-slip boundary condition at the reef surfaces by adjusting the velocity near the bottom**
263 **to satisfy the logarithmic law of the wall.**

264 Structured mesh is used to discretize the computational domain. The discretization is
265 kept constant in spanwise (y) direction (one layer of 20 mm/10 mm for Roeber/Yao et
266 al.’s scenarios) while it varies in streamwise (x) direction to reduce the number of the
267 total cells. From the left boundary to the toe of the fore-reef slopes, Δx decreases
268 gradually from 100 mm/24 mm to 20 mm/8 mm for Roeber/Yao et al.’s scenarios (see
269 e.g., Figs. 2b and 2c). The core region (see e.g., Fig. 2d), covering from the fore-reef
270 slope to the back-reef wall or beach, maintains constant cell sizes of $\Delta x = 20$ mm and 8

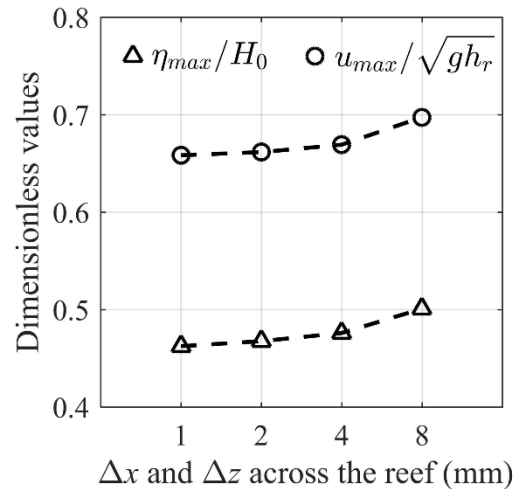
271 mm for the two experiments, respectively. Grid refinement near the free surface (e.g.,
 272 Figs. 2b and 2c) is conducted at the core region in x direction by reducing the grid sizes
 273 to one-quarter of their original values, e.g., $\Delta x = 5 \text{ mm}/2 \text{ mm}$. For the vertical (z)
 274 direction, the grid size is initially set to be $\Delta z = 20 \text{ mm}/8 \text{ mm}$ across the domain for
 275 Roeber/Yao et al.'s scenarios. Grid refinement near the free surface (e.g., Figs. 2b and 2c)
 276 is also conducted across the domain by reducing the grid sizes to $\Delta z = 5 \text{ mm}/2 \text{ mm}$. The
 277 total computational mesh consists of 4.87 million/1.18 million cells for Roeber/Yao et
 278 al.'s scenarios. The simulation duration is appointed to be 80 sec/30 sec to guarantee the
 279 arrival of the reflected waves at the most offshore wave gauge in both experiments. The
 280 time step is automatically adjusted during computation for a constant Courant number of
 281 0.25. Via parallel computing, it takes approximately 16d /2d for Roeber/Yao et al.'s
 282 scenarios on a cluster server with 44 CPUs (Intel Xeon, E5-2696, 2.2 G). No notable
 283 improvement of the results could be found with further refinement of the grid size.
 284



285 Fig. 2 Numerical grids and boundary conditions of the numerical domain.

286 For LES modelling solitary wave breaking over reefs, it is crucial to examine the
 287 Reynolds number (Re) at the incipient breaking point where strong turbulence is
 288 generated. It could be calculated by $Re = u_b (H_b + h_b) / \nu$ with $u_b = c_b H_b / h_b$ and
 289 $c_b = \sqrt{g (H_b + h_b)}$, where H_b , h_b , u_b and c_b are wave height, water depth, streamwise
 290 velocity and wave celerity at the breaking point, respectively. Re is estimated for all
 291 tested scenarios by using $H_b = H_0$ and $h_b = h_r$ (i.e., ignoring wave shoaling on the fore-
 292 reef slope and assuming wave breaking at the reef edge) and the values are also given in
 293 Table 1. Since the near-wall eddies are not resolved in this study, the total required grid

294 number is independent of Re (Pope, 2000). Ideal grid size of the LES model should be
 295 down to the Kolmogorov scale which is infeasible due to the limitation of computational
 296 resources. To test the convergence of grid size, we take the experiment with smaller wave
 297 flume (i.e., Scenario 3 in Table 1) which requires finer grid resolution as an example. We
 298 only examine the grid across the reef profile (the aforementioned core region) where the
 299 effect of grid size is supposed to be most influential. Both grid sizes (Δx and Δz) ranging
 300 from 8 mm down to 1 mm are tested. The results in terms of the dimensionless free
 301 surface elevation and streamwise velocity associated with the leading solitary wave in the
 302 inner reef flat (G7) are compared in Fig. 3. Only less than 2% differences in terms of
 303 wave and flow could be observed with the grid size varying from 2 mm to 1 mm,
 304 indicating that our selection of grid size $\Delta x = \Delta z = 2$ mm is sufficient for the current
 305 simulations.



306
 307 Fig. 3 Variation of the maximum dimensionless free surface elevation ($\eta_{max} / H_0 > 1$) and
 308 streamwise velocity ($u_{max} / \sqrt{gh} > 1$) at G7 with the grid size (Δx and Δz) across the
 309 reef for Case 3 in Table 1.

310
 311 To evaluate the performance of the model, the model skill value is adopted and
 312 calculated by Wilmott (1981)

313

$$skill = 1 - \frac{\sum |Y_{model} - Y_{obs}|^2}{\sum (|Y_{model} - \overline{Y_{obs}}| + |Y_{obs} - \overline{Y_{obs}}|)^2} \quad (14)$$

314

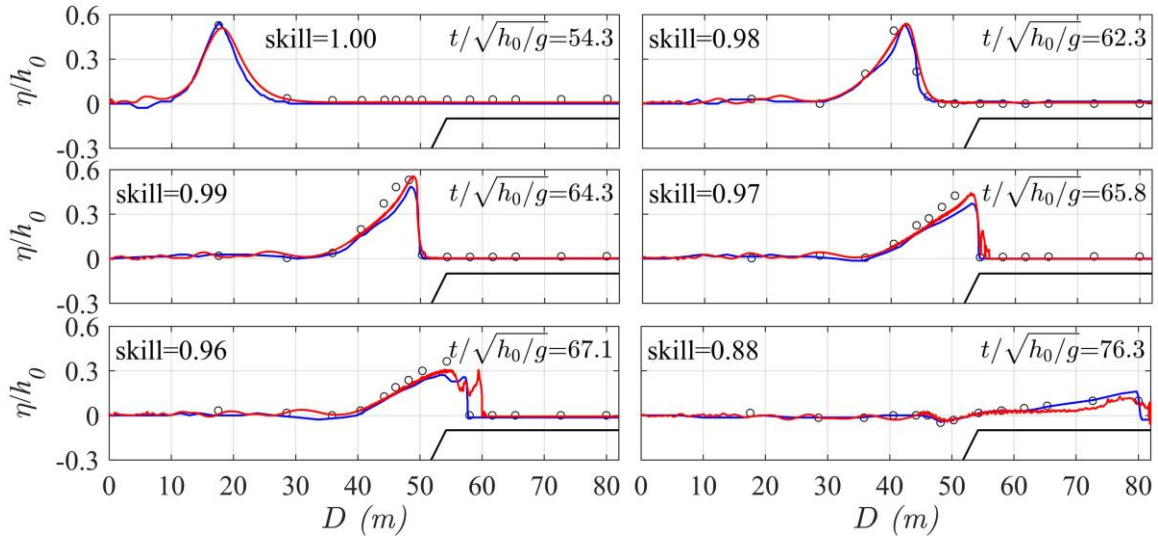
where Y_{model} is the predicted value, Y_{obs} is the measured value. The upper dash indicates
315 that the average value is taken. The higher the skill number (close to 1), the better
316 performance of the numerical model.

317

3.3 Comparison between numerical and experimental results

318

Fig. 4 compares the computed and the measured cross-shore distribution of the free
319 surface elevations (η) at different stages (t) for Scenario 1, where η is normalized by
320 the offshore still water depth (h_0) and t is normalized by $\sqrt{h_0/g}$. Incident solitary wave
321 gets steepened on the fore-reef slope at $t/\sqrt{h_0/g} = 62.3$ due to the shoaling effect. Then
322 its front becomes vertical prior to breaking at $t/\sqrt{h_0/g} = 64.3$. At $t/\sqrt{h_0/g} = 65.8$, a
323 plunging breaker occurs with air entrainment and splash-up near the reef edge. After that,
324 breaking wave starts to travel on the reef flat in the form of a propagating turbulent bore
325 at $t/\sqrt{h_0/g} = 67.1$. The bore shows a gradual reduction in amplitude and continues to
326 propagate downstream on the reef flat at $t/\sqrt{h_0/g} = 76.3$. The numerical results
327 generally agree well with the laboratory measurements at all stages with the skill values
328 larger than 0.85, indicating the robustness of the adopted model to address the solitary
329 wave processes across the laboratory reef profile in the large wave flume. When
330 comparing the predictions between our Navier-Stokes-equation-based model and a
331 Boussinesq model adopted by Roeber (2010), it seems that our model better captures the
332 steep near breaking wave ($t/\sqrt{h_0/g} = 64.3$) and breaking wave ($t/\sqrt{h_0/g} = 65.8$).



333

334 **Fig. 4** Dimensionless free surface elevations (η/h_0) across the reef at different stages

335 ($t/\sqrt{h_0/g}$) for Scenario 1. Red lines - present simulations; Blue lines - simulations from

336 Roeber (2010); Open circles - measurements from Roeber (2010); Skill values are for the

337 present simulations.

338

339 **Fig. 5** illustrates the computed and measured time-series of dimensionless free
 340 surface elevations (η/h_0) at different cross-shore locations (D) for Scenario 1. It

341 appears that the model reasonably simulates the transformation processes of solitary wave

342 on the fore-reef slope ($D = 35.9$ m and 44.3 m) and near the reef edge ($D = 50.4$ m)

343 with the skill values larger than 0.9. The skill values become relatively lower right after

344 the incipient wave breaking point ($D = 57.9$ m) and at the central reef flat ($D = 65.2$ m).

345 Such discrepancies may be primarily due to the air entrainment in measuring both the

346 breaking wave and the moving bore (Roeber, 2010) as well as the air bubble effect on

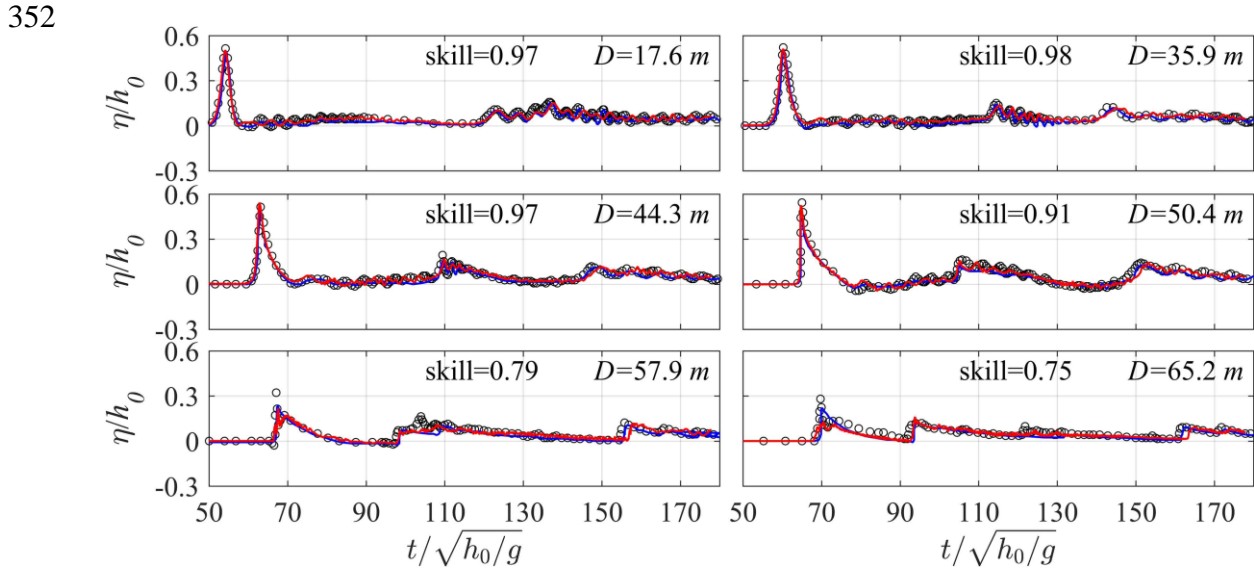
347 free surface tracking by the VOF method. In addition, the second peaks in the time series

348 are due to wave reflection from the back-reef wall, which are well predicted by the

349 present model. Meanwhile, no notable difference could be found in view of the time-series

349 predictions between the present model and the model of Roeber (2010), except at

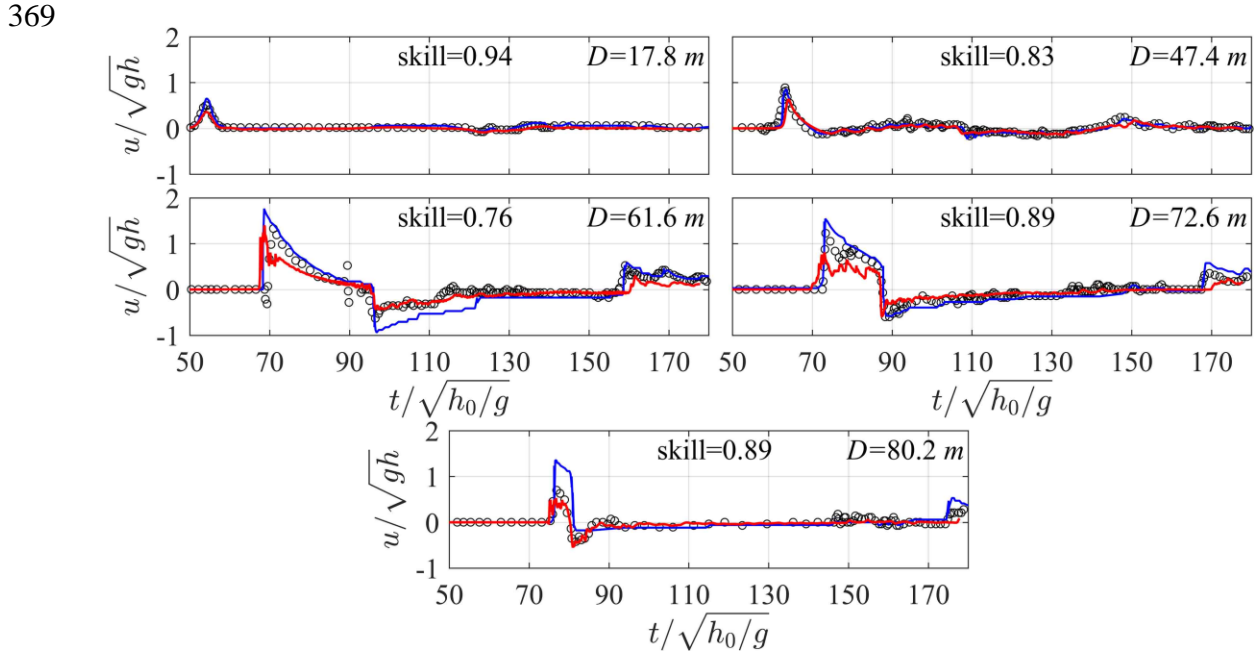
350 $D = 65.2$ m where the bore amplitude decays in our simulation compared to that at
 351 $D = 57.9$ m.



353 **Fig. 5** Time-series of dimensionless free surface elevations (η/h_0) at different cross-
 354 shore distances from the wavemaker (D) for Scenario 1. Red lines - present simulations;
 355 Blue lines - simulations from Roeber (2010); Open circles - measurements from Roeber
 356 (2010); Skill values are for the present simulations.

357 **Fig. 6** depicts the time-series of streamwise velocity (u) at five cross-shore
 358 locations (D) for Scenario 1, in which u is normalized by the local shallow water wave
 359 speed (\sqrt{gh}). The model satisfactorily captures the measured velocity offshore
 360 ($D = 17.8$ m), on the fore-reef slope ($D = 47.4$ m), on the central reef flat ($D = 72.6$ m)
 361 and near the shoreline ($D = 80.2$ m). A transition from the subcritical flow ($u/\sqrt{gh} < 1$)
 362 to supercritical flow ($u/\sqrt{gh} > 1$) could be observed right after wave breaking
 363 ($D = 61.6$ m), and less satisfactory prediction (skill values = 0.76) at this location is
 364 probably again due to both the effect of air-bubbles on both flow measurements in the
 365 experiments and free surface tracking in the simulations. Overall, the adopted model

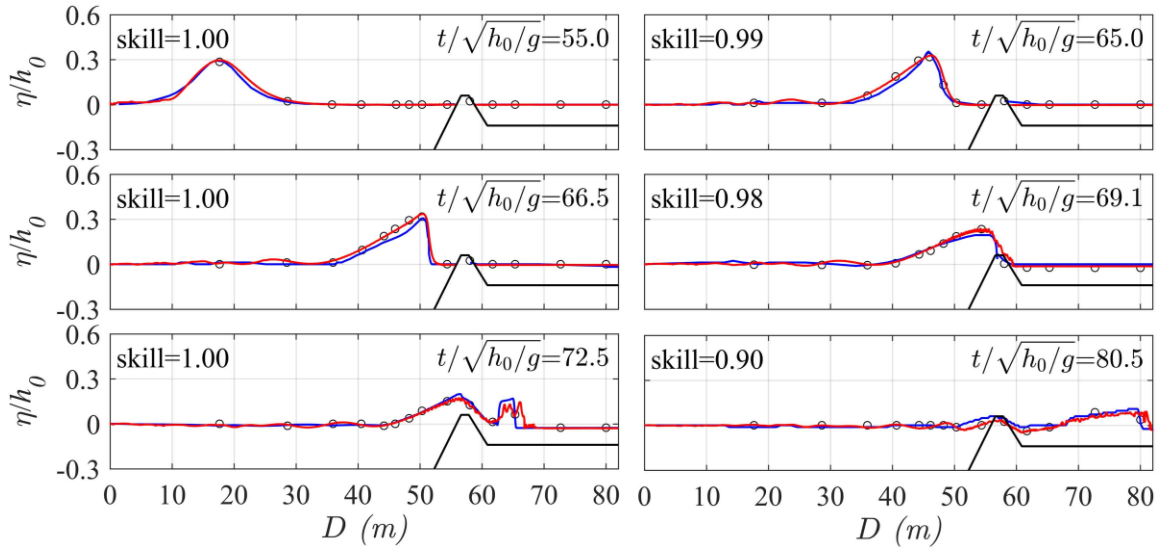
366 outperforms the Boussinesq model of Roeber (2010) in view of the velocity predictions,
 367 particularly both near the breaking point ($D = 61.6$ m) and the shoreline on the reef flat
 368 ($D = 80.2$ m).



370 **Fig. 6** Time-series of dimensionless streamwise velocity (u/\sqrt{gh}) at different cross-
 371 shore distances from the wavemaker (D) for Scenario 1. Red lines - present simulations;
 372 Blue lines - simulations from Roeber (2010); Open circles - measurements from Roeber
 373 (2010); Skill values are for the present simulations.

374 As previously introduced, the reef profile of Scenario 2 is identical to that of
 375 Scenario 1 except for a reef crest locating at the reef edge. The cross-shore distribution of
 376 dimensionless free surface elevations (η/h_0) at different stages ($t/\sqrt{h_0/g}$) for Scenario
 377 2 is demonstrated in **Fig. 7**. Steepened shoaling wave on the fore-reef slope appears at
 378 $t/\sqrt{h_0/g} = 65.0$ and its front becomes almost vertical prior to breaking at
 379 $t/\sqrt{h_0/g} = 66.5$. Breaking wave begins to overtop over the reef crest ($t/\sqrt{h_0/g} = 69.1$),
 380 and it then collapses on the leeside of reef crest, resulting in a moving turbulent bore

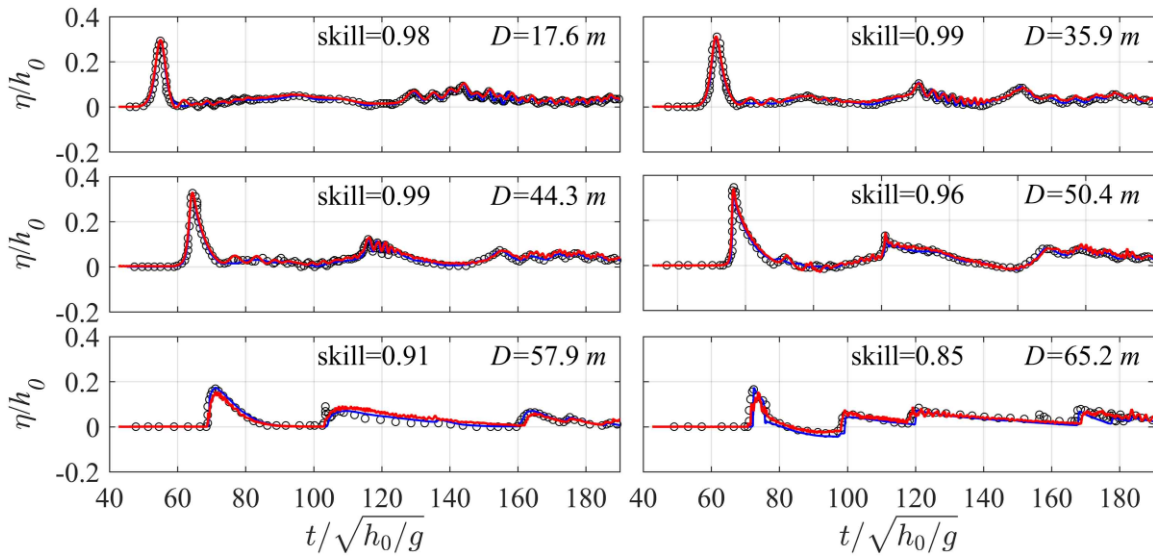
381 ($t/\sqrt{h_0/g} = 72.5$). The bore travels shoreward on the reef flat with the continuous
 382 damping of its magnitude ($t/\sqrt{h_0/g} = 80.5$). The skill values for all sampling locations
 383 in this Scenario are larger than 0.9, implying that the adopted model is able to well
 384 address the solitary wave processes over a more complicated reef geometry such as the
 385 presence of a reef crest at the reef edge. Again, the present model predicts the near
 386 breaking wave ($t/\sqrt{h_0/g} = 66.5$) and breaking wave ($t/\sqrt{h_0/g} = 69.1$ and
 387 $t/\sqrt{h_0/g} = 72.5$) slightly better than the model adopted by Roeber (2010).



388
 389 **Fig. 7** Dimensionless free surface elevations (η/h_0) across the reef at different stages
 390 ($t/\sqrt{h_0/g}$) for Scenario 2. Red lines - present simulations; Blue lines - simulations from
 391 Roeber (2010); Open circles - measurements from Roeber (2010); Skill values are for the
 392 present simulations.

393 **Fig. 8** compares the measured and simulated times-series of dimensionless free
 394 surface elevations (η/h_0) at various cross-shore locations (D) for Scenario 2. The skill
 395 values at all locations are larger than 0.85. It suggest again that the present model not
 396 only reasonably reproduces wave propagation offshore ($D = 17.6$ m), shoaling on the

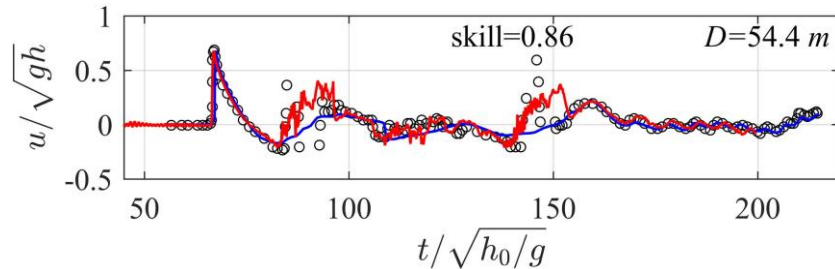
397 fore-reef slope ($D = 35.9$ m and 44.3 m) and near breaking in front of the reef crest
 398 ($D = 50.4$ m), breaking-wave transformation over the reef crest ($D = 57.9$ m), and bore
 399 evolution on the reef flat ($D = 65.2$ m), but also captures the tail waves caused by wave
 400 reflection from the back-reef wall (see e.g., $D = 65.2$ m). Overall, both our model and
 401 the model of Roeber (2010) reproduce the timeseries of free surface elevations equally
 402 well for this scenario.



403
 404 **Fig. 8** Time-series of dimensionless free surface elevations (η/h_0) at different cross-
 405 shore distances from the wavemaker (D) for Scenario 2. Red lines - present simulations;
 406 Blue lines - simulations from Roeber (2010); Open circles - measurements from Roeber
 407 (2010); Skill values are for the present simulations.

408 As for Scenario 2, Roeber (2010) only reported one location of flow measurement
 409 on the seaside face of the reef crest. **Fig. 9** presents the time-series of dimensionless
 410 streamwise velocity (u/\sqrt{gh}) at the point ($x = 54.4$ m), and a skewed and peaky
 411 velocity profile is observed associated with the leading solitary wave because the position
 412 is very close to the incipient wave breaking point. The two secondary peaks in the time
 413 series are generated by the reflected waves from the reef crest and from the back-reef
 414 wall, respectively. The model captures the temporal variation of current fairly well with

415 the skill value of 0.86, and its prediction is also better than that from the model of Roeber
 416 (2010), particularly for the reflected waves.
 417

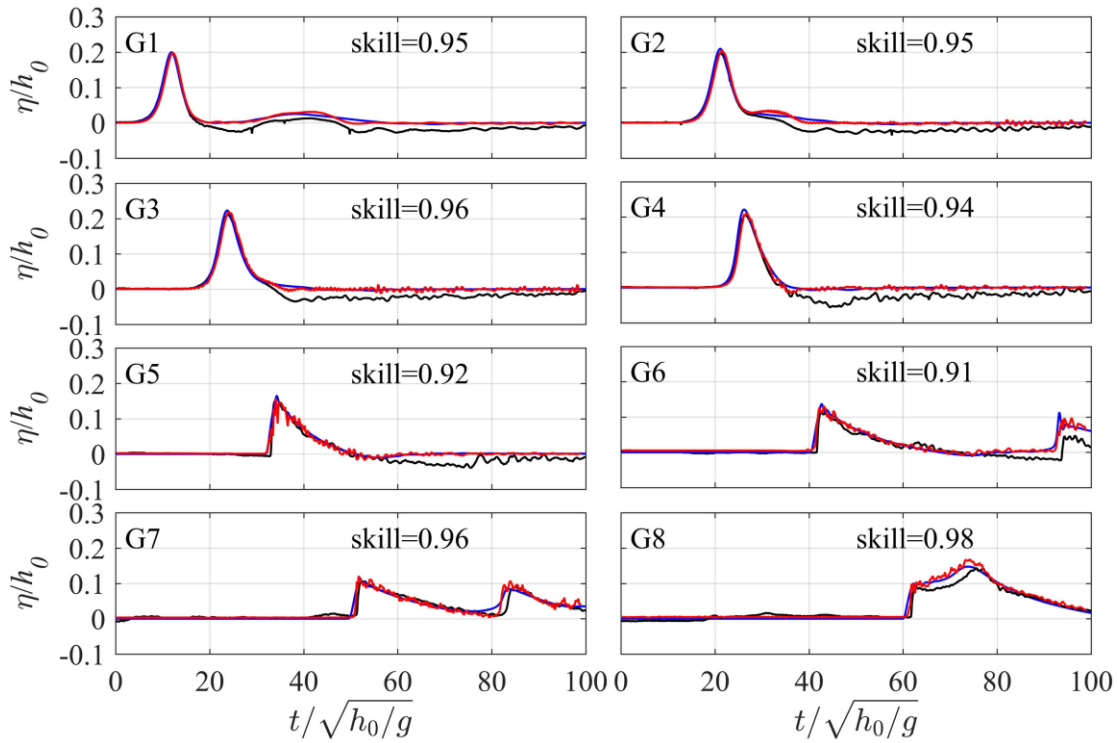


418 **Fig. 9** Time-series of dimensionless streamwise velocity (u/\sqrt{gh}) at the cross-shore
 419 distance $D = 54.4$ m from the wavemaker for Scenario 2. Red lines - present simulations;
 420 Blue lines - simulations from Roeber (2010); Open circles - measurements from Roeber
 421 (2010); Skill values are for the present simulations.
 422

423 The experiments of Yao et al. (2018) only measured the timeseries of wave records
 424 at limited locations (G1-G8) across the reef as well as the maximum wave runup on the
 425 final beach. **Fig. 10** compares the computed and measured time-series free surface
 426 elevations for Scenario 3. The overall agreement between the simulations and
 427 experiments for G1-G8 is very good with the skill values at all locations larger than 0.9.
 428 When the solitary wave travels from the toe (G2) to the middle of fore-reef slope (G3), it
 429 gets steepened due to the shoaling effect. Wave breaking starts at a location right before
 430 the reef edge (G4) and the surfzone processes extend over the reef flat in the form of a
 431 moving bore. Thus from G5 to G8, the wave timeseries show saw-shaped profiles and
 432 there is a cross-shore decrease of the leading solitary wave height. Such features of the
 433 breaking waves are also well captured by the model. Note that the second peak in the
 434 timeseries of G7 is due to wave reflection from the back-reef beach, and the incident and
 435 reflected waves are not fully separated from each other at G8 because this location is too
 436 close to the beach. The predicted and measured wave runups are 0.122 m and 0.109 m,
 respectively, for this scenario. Compared to the Boussinesq model employed by Yao et al.

437
438

(2018), no significant difference in the predicted timeseries could be found for the present Navier-Stokes-equation-based model.

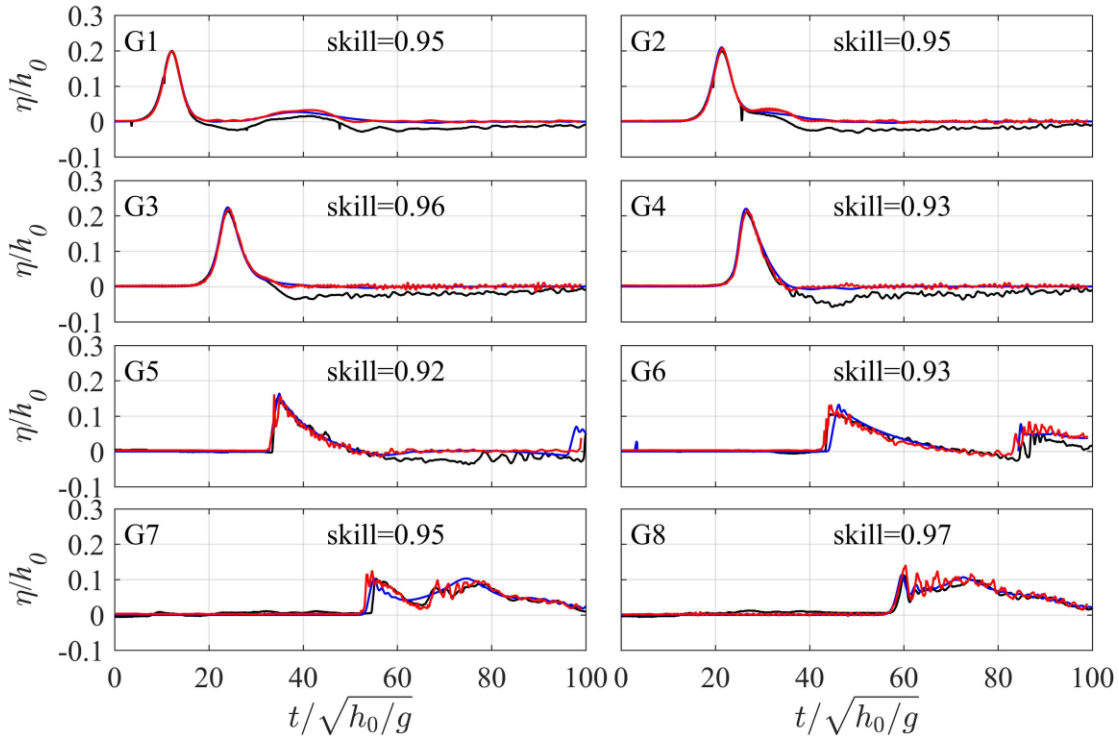


439

440 **Fig. 10** Time-series of dimensionless free surface elevations (η/h_0) at different cross-
441 shore sampling locations (G1-G8) for Scenario 3. Red lines - present simulations; Blue
442 lines - simulations from Yao et al. (2008); Black lines - measurements from Yao et al.
443 (2008); Skill values are for the present simulations.
444

445 **Fig. 11** depicts the same comparison of wave time-series but for the reef profile with
446 a lagoon (Scenario 4). Again, the model performance for this scenario is fairly good (all
447 skill values larger than 0.9). The predicted and measured wave runups are 0.123 m and
448 0.116 m, respectively, for this scenario. Notable mismatch only appears for those small
449 wave oscillations generated by the reflected wave propagating out of the lagoon to the
450 reef flat (i.e., from G8 to G6). But our model seems to be superior to the model of Yao et
451 al. (2018) to reproduce those oscillations at G7 and G8. We finally remark that the tail of
leading solitary wave, particularly from G1 to G4, is below the initial water level in the

452 laboratory data, which is due to the water lost to form the generated wave crest around
 453 the paddle of the wave maker. However, such phenomenon is not observed in the
 454 numerical results because we generate a theoretical solitary wave in the numerical
 455 domain as indicated by Eq. (11).



456
 457 **Fig. 11** Time-series of dimensionless free surface elevations (η/h_0) at different cross-
 458 shore sampling locations (G1-G8) for Scenario 4. Red lines - present simulations; Blue
 459 lines - simulations from Yao et al. (2008); Black lines - measurements from Yao et al.
 460 (2008); Skill values are for the present simulations.

461 **4. Model Applications**

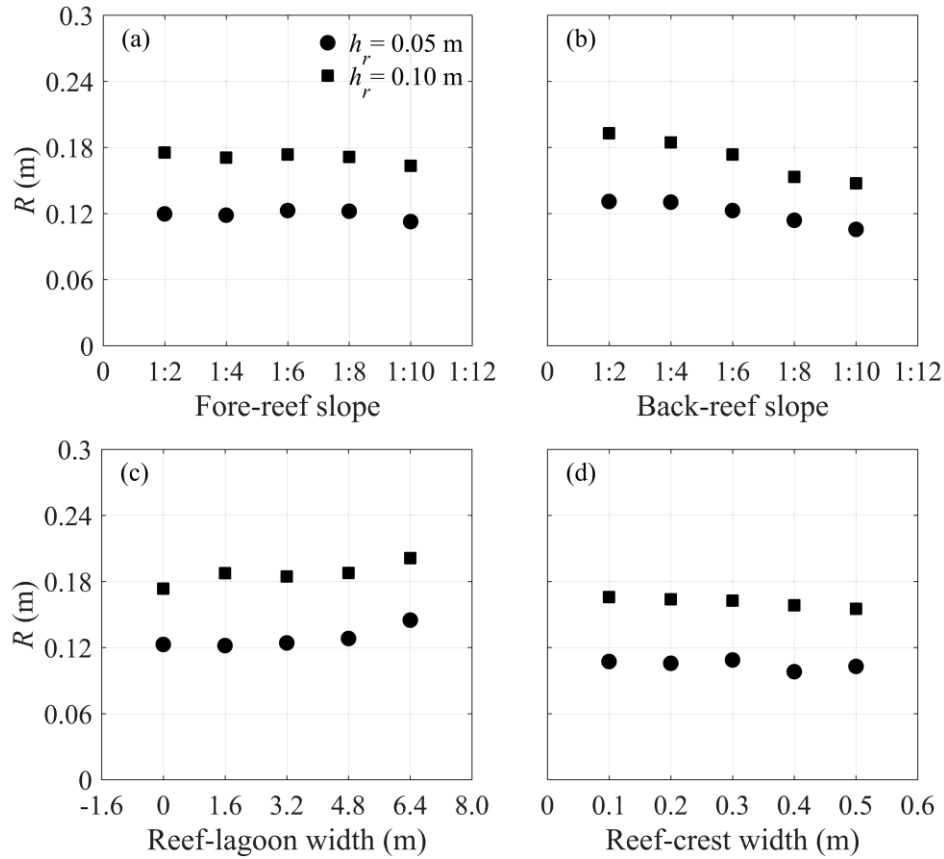
462 **4.1 Effects of reef morphology variations on the solitary wave runup**

463 In this section, we apply the well-validated LES model to examine the variations of
 464 reef morphological parameters (fore-reef slope, back-reef slope, lagoon width, reef-crest
 465 width) that may affect the wave runup (R) on the back-reef beach. Based on Scenario 3
 466 (1: 6 for both the slopes of fore-reef and back-reef, 9.6 m for the reef length, no reef crest
 467 and no lagoon) from Yao et al. (2018), we firstly test five slopes (1:2, 1:4, 1:6, 1:8 and

468 1:10, which all fall within the common range of 1:1 to 1:20 in the reported field
469 observations, see e.g., Quataert et al. 2015, their Table 1) for both the fore-reef and the
470 back-reef. We then consider the existence of a lagoon at the rear of reef flat by testing
471 four upper widths of the lagoon (1.6 m, 3.2 m, 4.8 m and 6.4 m) and comparing to the
472 case without lagoon (lagoon width=0 m). We finally investigate a trapezoidal reef crest
473 locating at the reef edge with its seaward slope matching the fore-reef slope and its
474 shoreward slope of 1:1. We examine five reef-crest widths (0.1 m, 0.2 m, 0.3 m, 0.4 m
475 and 0.5 m) in view that the dimension of reef crest at the field scale is on the magnitude
476 of meters (see e.g., Hench et al., 2008). During simulations, each run is performed by
477 changing one of above morphological parameters while keeping other parameters
478 unaltered. All runs are conducted under a combination of one solitary wave height
479 ($H_0 = 0.08$ m) and two reef-flat water depths ($h_r = 0.05$ m and $h_r = 0.1$ m).

480 Generally, Fig. 12a shows that R is not very sensitive to the change of the fore-reef
481 slope within the tested range, in that wave breaking for this scenario occurs closely to the
482 reef edge (G4), thus most of the surfzone processes and associated energy dissipation
483 complete on the reef flat. Only when the fore-reef slope becomes steeper than 1:8, R
484 decreases slightly under both water depths (h_r), which is attributed to the increased fore-
485 reef reflection of the incident wave energy. Fig. 12b reveals that R is more sensitive to
486 the back-beach slope under both h_r . It decreases significantly as the back-beach slope
487 becomes milder, which is consistent with that found for the plane slope (see e.g.,
488 Synolakis, 1987). Fig. 12c shows the variation of R with the lagoon width. Note that the
489 zero width represents the reef without lagoon. It appears that R increases notably with
490 the increase of lagoon width because a wider lagoon dissipates less wave energy partly
491 due to the stoppage of propagating bore and partly due to the reduction of bottom friction.
492 As for the effect of reef-crest width (Fig. 12d), although the presence of a reef crest is
493 reported to be an important factor affecting the wind wave transformation over fringing
494 reefs (e.g., Yao et al., 2017), it seems to have little impact on the solitary wave runup
495 under both h_r , slight decline of R could only be found under the crest width larger than
496 0.4. This is because the solitary wave is very long compared to the reef-crest width, thus
497 most of its energy could transmit over the narrow reef crest. However, when the reef crest

498 becomes sufficient wide, its shallower crest tends to energize the wave breaking thus the
 499 energy dissipation. To summarize all above analyses, it can be concluded that coastal
 500 regions protected by the fringing reefs with steeper back-reef slopes and wider lagoons
 501 are more valuable to coastal inundation during a tsunami event.

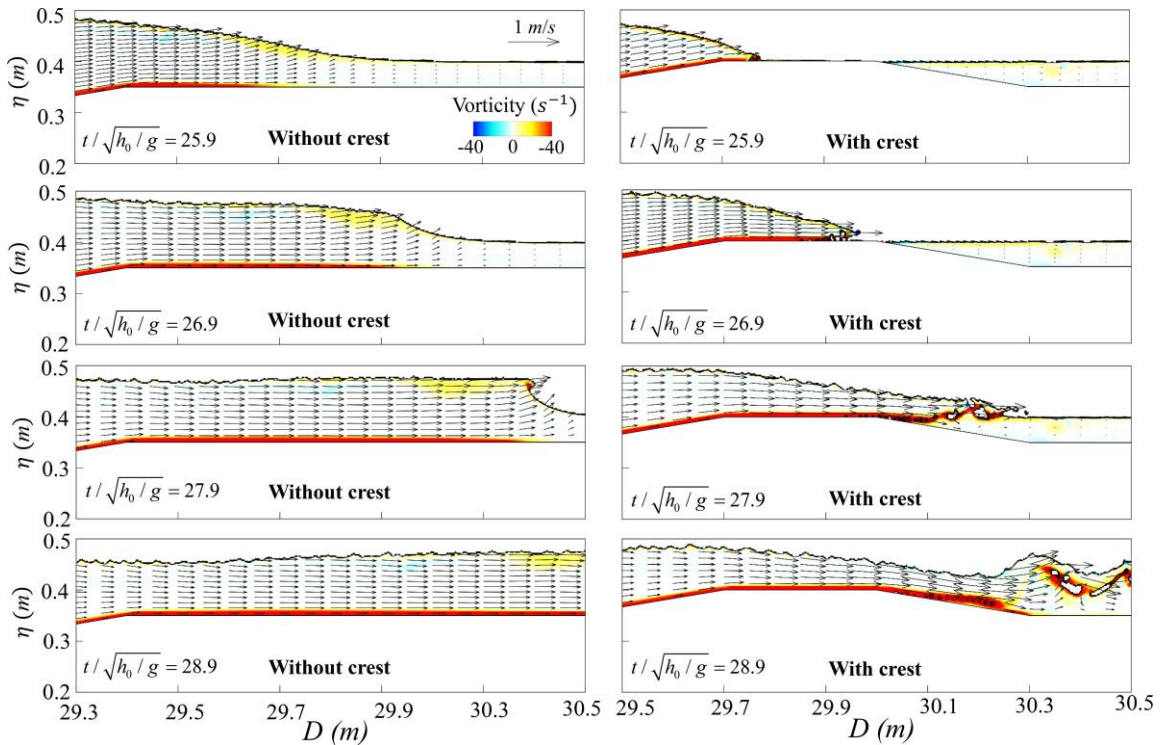


502
 503 **Fig. 12** The predicted wave runup on the back-reef beach (R) under $H_0 = 0.08$ m **with**
 504 **varying:** (a) fore-reef slopes; (b) back-reef slopes; (c) lagoon widths; and (d) reef-crest
 505 widths.

506 4.2 Wave-driven current and vortices around the reef crest and the lagoon

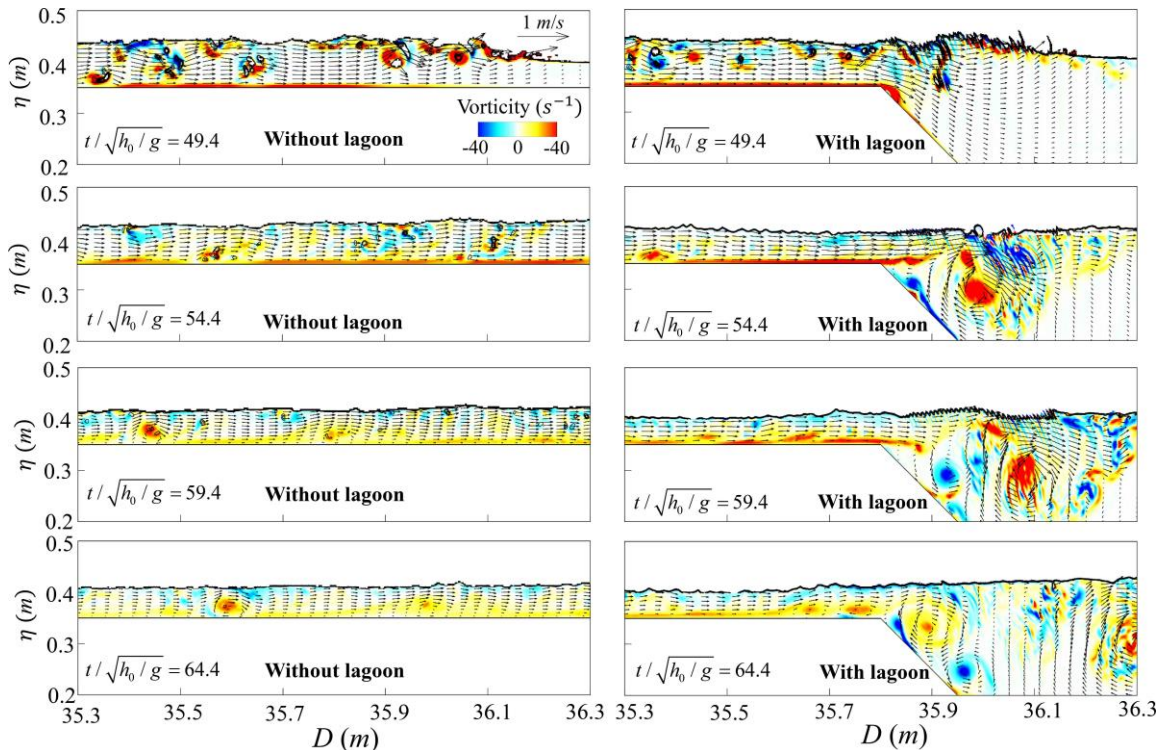
507 One advantage of the current Navier-Stokes-equation-based model over the depth-
 508 integrated models is its ability to resolve the vertical flow structure under breaking waves,
 509 particularly around the complex reef geometry. Based on the reef profile of Yao et al.
 510 (2018), **Fig. 13** shows the simulated wave-driven current and vorticity on the x-z plane at
 511 different stages ($t/\sqrt{h_0/g}$) for the reefs with and without a reef crest at the reef edge
 512 subjected to the same solitary wave condition ($H_0 = 0.08$ m and $h_r = 0.05$ m). Without

513 the reef crest, shoaling wave propagates onto the horizontal reef flat with a uniform
 514 velocity distribution underneath ($t/\sqrt{h_0/g} = 25.9$ and 26.9), which is typical for the
 515 shallow-water long waves. Until to $t/\sqrt{h_0/g} = 27.9$, wave breaking occurs in the form
 516 of a plunging breaker, and vortex generation gathers mainly around the wave crest. The
 517 vortices are transported further downstream at $t/\sqrt{h_0/g} = 28.9$. When the wave crest
 518 exists, incipient wave breaking moves seaward and it takes place at the seaside edge of
 519 the reef crest ($t/\sqrt{h_0/g} = 25.9$). The breaker then overtops over the reef crest
 520 ($t/\sqrt{h_0/g} = 26.9$) and plunges onto the reef flat leeside of the reef crest, resulting a
 521 hydraulic jump ($t/\sqrt{h_0/g} = 27.9$). Consequently, wave-driven current at the rear part of
 522 the reef crest is dramatically increased compared to the same location without the crest.
 523 Both the intensity and the extent of vortex generation are also enlarged at the leeside of
 524 the reef crest ($t/\sqrt{h_0/g} = 28.9$), leading to increased wave energy dissipation compared
 525 to the case without the reef crest.



526
 527 **Fig. 13** Comparison of wave-driven current and vorticity on the x-z plane at different
 528 stages ($t/\sqrt{h_0/g}$) between the reefs with and without the reef crest ($H_0 = 0.08$ m and
 529 $h_r = 0.05$ m).

530 **Fig. 14** compares the computed wave-driven current and vorticity on the x-z plane
 531 at different stages ($t/\sqrt{h_0/g}$) between the reefs in the presence and absence of the
 532 lagoon. Without the lagoon, the propagating bore arrives with strong vortex motions
 533 ($t/\sqrt{h_0/g}=49.4$). The vortices are eventually transported downstream from
 534 $t/\sqrt{h_0/g}=54.4$ to 64.4. However, when the lagoon is present, the current speed over
 535 the depth slows down and additional vortices generate at the seaside edge of the lagoon as
 536 the bore propagates into the lagoon ($t/\sqrt{h_0/g}=49.4$). The peak value of the vorticity
 537 appears at a later time ($t/\sqrt{h_0/g}=54.4$). After that, the vortices in the lagoon are
 538 primarily diffused by the vortex shedding ($t/\sqrt{h_0/g}=59.4$ and 64.4). Compared to the
 539 case without the lagoon, although the existence of a lagoon dissipates less wave energy
 540 by terminating the propagating bore and reducing the reef-flat friction as previously
 541 stated, the vortex generation and diffusion in the lagoon as demonstrated here is believed
 542 to cause local energy loss. We finally remark that the wave-driven current and vortices
 543 examined in this section could provide a first step to analyze more sophisticated problems,
 544 such as the tsunami-induced sediments/debris transport over the fringing reefs.



545

546 **Fig. 14** Comparison of wave-driven current and vorticity on the x-z plane at different
547 stages ($t / \sqrt{h_0 / g}$) between the reefs with and without the lagoon ($H_0 = 0.08$ m and
548 $h_r = 0.05$ m).

549 **5 Conclusions**

550 To remedy the inadequacies of using the depth-integrated models to simulate the
551 interaction between tsunami-like solitary waves and fringing reefs, a 3D numerical wave
552 tank, solving the Navier-Stokes equations with the LES for turbulence closure, has been
553 developed based on the open-source CFD tool OpenFOAM®. The free surface is tracked
554 by the VOF method. Two existing laboratory experiments with the wave, flow and wave
555 runup measurements based on different fringing reef profiles are employed to validate the
556 numerical model. Simulations show that the current Navier-Stokes-equation-based model
557 outperforms the commonly used Boussinesq-typed models in view of its capability to
558 better reproduce the breaking waves and wave-driven current on the reef flat. The model
559 is then applied to investigate the impacts of varying morphologic features on the back-
560 reef wave runup. The flow and vorticity fields associated with the breaking solitary wave
561 around the reef crest and the lagoon are also analyzed via the numerical simulations.

562 Model results shows that wave runup on the back-reef slope is most sensitive to the
563 variation of the back-reef slope, less sensitive to the lagoon width, and almost insensitive
564 to the variations of both the fore-reef slope and the reef-crest width within our tested
565 ranges. The existence of a reef crest or a lagoon can notably alter the wave-driven current
566 and vortex evolutions on the reef flat. These findings demonstrate that low-lying coastal
567 areas fringed by coral reefs with steep back-reef slopes and larger lagoons are expected to
568 experience larger wave runup near the shoreline, thus they are more susceptible to the
569 coastal inundation during a tsunami event.

570

571

572 **Acknowledgements**

573 This study was supported financially by the National Natural Science Foundation of
574 China (grant nos.51679014 and 11702244), the Hunan Science and Technology Plan
575 Program (Grant No. 2017RS3035), and the Open Foundation of Key Laboratory of
576 Coastal Disasters and Defense of Ministry of Education (grant no.201602).

577 **References**

- 578 Chatenoux, B., and Peduzzi, P.: Impacts from the 2004 Indian Ocean Tsunami: analysing
579 the potential protecting role of environmental features, *Nat. Hazards*, 40, 289–304,
580 2007.
- 581 Cheriton, O. M., Storlazzi, C. D., and Rosenberger, K. J.: Observations of wave
582 transformation over a fringing coral reef and the importance of low-frequency waves
583 and offshore water levels to runup, overwash, and coastal flooding, *J. Geophys. Res.*
584 *Oceans*, 121, 3121–3140, <https://doi:10.1002/2015JC011231>, 2016.
- 585 Craik, A. D., and Leibovich, S.: A rational model for Langmuir circulations. *J. Fluid*
586 *Mech*, 73(3), 401–426, 1976.
- 587 Dahdouh-Guebas, F., Koedam, N., Danielsen, F., Sørensen, M. K., Olwig, M. F., Selvam,
588 V., Parish, F., Burgess, N. D., Topp-Jørgensen, E., Hiraishi, T., Karunakaran, V. M.,
589 Rasmussen, M. S., Hansen, L. B., Quarto, A., and Suryadiputra, N.: Coastal
590 vegetation and the asian tsunami, *Science*, 311, 37–38, 2006.
- 591 Danielsen, F., Sørensen, M. K., Olwig, M. F., Selvam, V., Parish, F., Burgess, N. D.,
592 Hiraishi, T., Karunakaran, V. M., Rasmussen, M. S., Hansen, L. B., Quarto, A., and
593 Suryadiputra, N.: The asian tsunami: a protective role for coastal vegetation, *Science*,
594 310, 643–643, 2005.
- 595 Dongeren, A. V., Lowe, R., Pomeroy, A., Trang, D. M., Roelvink, D., Symonds, G., and
596 Ranasinghe, R.: Numerical modeling of low-frequency wave dynamics over a
597 fringing coral reef, *Coastal Eng.*, 73, 178–190, 2013.
- 598 Douillet, P., Ouillon, S., and Cordier, E.: A numerical model for fine suspended sediment
599 transport in the southwest lagoon of New Caledonia, *Coral Reefs*, 20, 361–372,
600 2001.
- 601 Ford, M., Becker, J. M., Merrifield, M. A., and Song, Y. T.: Marshall islands fringing reef
602 and atoll lagoon observations of the Tohoku Tsunami, *Pure Appl. Geophys.*, 171,
603 3351–3363, 2014.
- 604 Gourlay, M. R.: Wave set-up on coral reefs. 2. Wave set-up on reefs with various profiles,
605 *Coastal Eng.*, 28, 17–55, 1996.
- 606 Hench, J. L., Leichter, J. J., and Monismith, S. G.: Episodic circulation and exchange in a
607 wave-driven coral reef and lagoon system, *Limnol. Oceanogr.*, 53, 2681–2694, 2008.

608 Higuera, P., Lara, J. L., and Losada, I. J.: Realistic wave generation and active wave
609 absorption for Navier–Stokes models application to OpenFOAM®, *Coastal Eng.*, 71,
610 102–118, 2013a.

611 Higuera, P., Lara, J. L., and Losada, I. J.: Simulating coastal engineering processes with
612 OpenFOAM®, *Coastal Eng.*, 71, 119–134, 2013b.

613 Hirt, C. W., and Nichols, B. D.: Volume of fluid (VOF) method for the dynamics of free
614 boundaries, *J. Comput. Phys.*, 39, 201–225, 1981.

615 Huang, Z., Yao, Y., Sim, S. Y., and Yao, Y.: Interaction of solitary waves with emergent,
616 rigid vegetation. *Ocean Eng.*, 38, 1080–1088, 2011.

617 Jacobsen, N. G., Fuhrman, D. R., and Fredsøe, J.: A wave generation toolbox for the
618 open–source CFD library: OpenFoam®, *Int. J. Numer. Meth. Fluids*, 70, 1073–1088,
619 2012.

620 Kraines, S. B., Yanagi, T., Isobe, M., and Komiyama, H.: Wind-wave-driven circulation
621 on the coral reef at Bora Bay, Miyako Island, *Coral Reefs*, 17, 133–143, 1998.

622 Kunkel, C. M., Hallberg, R. W., and Oppenheimer, M.: Coral reefs reduce tsunami impact
623 in model simulations. *Geophys. Res. Lett.*, 33, 265–288, 2006.

624 Lee, J. J., Skjelbreia, J. E., and Raichlen, F.: Measurement of velocities in solitary waves,
625 *J. Waterw. Port C-ASCE*, 108, 200–218, 1982.

626 Leonard, A.: Energy cascade in large-eddy simulations of turbulent fluid flows, *Adv.*
627 *Geophys.*, 18, 237–248, 1975.

628 Longuet-Higgins, M. S., and Stewart, R. W.: Radiation stresses in water waves; a
629 physical discussion, with applications, *Deep-Sea Res.*, 11, 529–562, 1964.

630 Lowe, R. J., Falter, J. L., Bandet, M. D., Pawlak, G., and Atkinson, M. J.: Spectral wave
631 dissipation over a barrier reef, *J. Geophys. Res.*, 110, C04001,
632 <https://doi:10.1029/2004JC002711>, 2005.

633 Lowe, R. J., Falter, J. L., Monismith, S. G., and Atkinson, M. J.: Wave-driven circulation
634 of a coastal reef-lagoon system, *J. Phys. Oceanogr.*, 39, 873–893, 2009a.

635 Lowe, R. J., Falter, J. L., Monismith, S. G., and Atkinson, M. J.: A numerical study of
636 circulation in a coastal reef-lagoon system, *J. Geophys. Res.*, 114, C06022,
637 <https://doi:10.1029/2008JC005081>, 2009b.

638 Lowe, R. J., Hart, C., and Pattiaratchi C. B.: Morphological constraints to wave-driven

639 circulation in coastal reef-lagoon systems: A numerical study, *J. Geophys. Res.*, 115,
640 C09021, <https://doi:10.1029/2009JC005753>, 2010.

641 Lugo-Fernandez, A., Roberts, H. H., and Suhayda, J. N.: Wave transformations across a
642 Caribbean fringing-barrier Coral Reef, *Cont. Shelf Res.*, 18, 1099–1124, 1998.

643 Maza, M., Lara, J. L., and Losada, I. J.: Tsunami wave interaction with mangrove forests:
644 a 3-d numerical approach, *Coastal Eng.*, 98, 33–54, 2015.

645 Mcadoo, B. G., Ah-Leong, J. S., Bell, L., Ifopo, P., Ward, J., Lovell, E., and Skelton, P.:
646 Coral reefs as buffers during the 2009 South Pacific Tsunami, Upolu Island, Samoa,
647 *Earth-Sci. Reviews*, 107, 147–155, 2011.

648 Menon, S., Yeung, P. K., and Kim, W. W.: Effect of subgrid models on the computed
649 interscale energy transfer in isotropic turbulence, *Comput. Fluids*, 25, 165–180,
650 1996.

651 Nwogu, O., and Demirbilek, Z.: Infragravity wave motions and run-up over shallow
652 fringing reefs, *J. Waterw. Port C.*, 136, 295–305, 2010.

653 OpenFOAM Foundation: OpenFOAM® User Guide, <http://www.openfoam.org>, (Nov. 25,
654 2016), 2013.

655 Péquignet, A. C., Becker, J. M., Merrifield, M. A., and Boc S. J.: The dissipation of wind
656 wave energy across a fringing reef at Ipan, Guam, *Coral Reefs*, 30, 71–82, 2011.

657 Pope, S. B.: *Turbulent flows*, Cambridge University Press, Cambridge, U.K., 2000.

658 Quataert, E., Storlazzi, C., Van Rooijen, A., Cheriton, O., and Van Dongeren, A.: The
659 influence of coral reefs and climate change on wave-driven flooding of tropical
660 coastlines, *Geophys. Res. Lett.*, 42, 6407–6415, <https://doi:10.1002/2015GL064861>,
661 2015.

662 Roeber, V.: Boussinesq-type mode for nearshore wave processes in fringing reef
663 environment, PhD Thesis, University of Hawaii at Manoa, Honolulu, HI, 2010.

664 Roeber, V., and Cheung, K. F.: Boussinesq-type model for energetic breaking waves in
665 fringing reef environments, *Coast. Eng.*, 70, 1–20, 2012.

666 Skotner, C., and Apelt, C. J.: Application of a Boussinesq model for the computation of
667 breaking waves, Part 2: wave-induced setdown and set-up on a submerged coral reef,
668 *Ocean Eng.*, 26, 927–947, 1999.

669 Synolakis, C. E.: The runup of solitary waves, *J. Fluid Mech.*, 185, 523–545, 1987.

670 Su, S. F., Ma, G., and Hsu, T. W.: Boussinesq modeling of spatial variability of
671 infragravity waves on fringing reefs, *Ocean Eng.*, 101, 78–92, 2015.

672 Su, S. F., and Ma, G.: Modeling two-dimensional infragravity motions on a fringing reef,
673 *Ocean Eng.*, 153, 256–267, 2018.

674 Tang, J., Causon, D., Mingham, C., and Qian, L., Numerical study of vegetation damping
675 effects on solitary wave run-up using the nonlinear shallow water equations, *Coastal*
676 *Eng.*, 75, 21–28, 2013.

677 Willmott, C. J.: On the validation of models, *Phys. Geogr.*, 2, 184–194, 1981.

678 Yao, Y., Huang, Z. H., Monismith, S. G., and Lo, E. Y. M.: 1DH Boussinesq modeling of
679 wave transformation over fringing reefs, *Ocean Eng.*, 47, 30–42, 2012.

680 Yao, Y., Du, R. C., Jiang, C. B., Tang, Z. J., and Yuan, W. C.: Experimental study of
681 reduction of solitary wave run-up by emergent rigid vegetation on a beach, *J. Earthq.*
682 *Tsunami*, 9, 1540003, 2015.

683 Yao, Y., Becker, J. M., Ford, M. R., and Merrifield, M. A.: Modeling wave processes over
684 fringing reefs with an excavation pit, *Coastal Eng.*, 109, 9–19, 2016.

685 Yao, Y., He, W. R., Du, R. C., and Jiang, C. B.: Study on wave-induced setup over
686 fringing reefs in the presence of a reef crest, *Appl. Ocean Res.*, 66, 164–177, 2017.

687 Yao, Y., He, F., Tang, Z. J., and Liu, Z. S.: A study of tsunami-like solitary wave
688 transformation and run-up over fringing reefs, *Ocean Eng.*, 149, 142–155, 2018.

689 Yao, Y., Zhang, Q. M., Chen, S. G, and Tang, Z. J.: Effects of reef morphology variations
690 on wave processes over fringing reefs, *Appl. Ocean Res.*, 82, 52–62, 2019.

691 Yoshizawa, A., and Horiuti, K.: A statistically-derived subgridscale kinetic energy model
692 for the large-eddy simulation of turbulent flows, *J. Phys. Soc. Jpn.*, 54, 2834–2839,
693 1985.

694 Young, I. R.: Wave transformations over coral reefs, *J. Geophys. Res.-Oceans*, 94, 9779–
695 9789, 1989.